Icarus 209 (2010) 818–835

Contents lists available at ScienceDirect

Icarus

journal homepage: www.elsevier.com/locate/icarus

Generation and emplacement of fine-grained ejecta in planetary impacts

Rebecca R. Ghent [a,*], V. Gupta [a], B.A. Campbell [b], S.A. Ferguson [a], J.C.W. Brown [a], R.L. Fergason [c], L.M. Carter [b]

[a] Department of Geology, University of Toronto, 22 Russell St., Toronto, ON, Canada M5S 3B1
[b] Center for Earth and Planetary Studies, Smithsonian Institution, Washington, DC 20013-7012, United States
[c] Astrogeology Science Center, USGS, Flagstaff, AZ 86001, United States

ARTICLE INFO

Article history:
Received 22 October 2009
Revised 7 May 2010
Accepted 11 May 2010
Available online 20 May 2010

Keywords:
Moon
Mars
Venus
Cratering
Radar observations

ABSTRACT

We report here on a survey of distal fine-grained ejecta deposits on the Moon, Mars, and Venus. On all three planets, fine-grained ejecta form circular haloes that extend beyond the continuous ejecta and other types of distal deposits such as run-out lobes or ramparts. Using Earth-based radar images, we find that lunar fine-grained ejecta haloes represent meters-thick deposits with abrupt margins, and are depleted in rocks $\geqslant$1 cm in diameter. Martian haloes show low nighttime thermal IR temperatures and thermal inertia, indicating the presence of fine particles estimated to range from ~10 μm to 10 mm. Using the large sample sizes afforded by global datasets for Venus and Mars, and a complete nearside radar map for the Moon, we establish statistically robust scaling relationships between crater radius R and fine-grained ejecta run-out r^* for all three planets. On the Moon, $r^* \sim R^{-0.18}$ for craters 5–640 km in diameter. For Venus, radar-dark haloes are larger than those on the Moon, but scale as $r^* \sim R^{-0.49}$, consistent with ejecta entrainment in Venus' dense atmosphere. On Mars, fine-ejecta haloes are larger than lunar haloes for a given crater size, indicating entrainment of ejecta by the atmosphere or vaporized subsurface volatiles, but scale as $R^{-0.13}$, similar to the ballistic lunar scaling. Ejecta suspension in vortices generated by passage of the ejecta curtain is predicted to result in ejecta run-out that scales with crater size as $R^{1/2}$, and the wind speeds so generated may be insufficient to transport particles at the larger end of the calculated range. The observed scaling and morphology of the low-temperature haloes leads us rather to favor winds generated by early-stage vapor plume expansion as the emplacement mechanism for low-temperature halo materials.

1. Introduction

On the terrestrial planets, impacts play a central role in generating and reworking regolith materials. On the Moon, the regolith consists almost entirely of overlapping impact ejecta deposits. On an airless body, processes that control the radial extent, total volume, and statistical distribution of particles in an ejecta deposit are limited to ballistic ejection and deposition, plus subsequent motion of material along the surface (e.g., by granular flow). For planets with atmospheres, emplacement is moderated by interaction between the atmosphere and individual ejecta, or an ejecta curtain. Here we present a survey of fine-grained ejecta deposits on the Moon, Venus, and Mars, focusing on both morphology and scaling. We establish relationships between crater size and maximum fine ejecta run-out for all three planets, and discuss the implications of our observed scaling for emplacement processes. The results presented here are significant because they provide the opportunity to constrain the mechanisms of production and emplacement of fragmentary impact debris. The spatial distribution of fine ejecta, and their particle size distribution, constrain important elements of the cratering process not accessible in laboratory experiments, such as block comminution and far-field deposition.

2. Fine ejecta deposits: morphology, thickness, and constituent particle size

2.1. Radar-dark haloes on the Moon

On the lunar nearside, radar-dark ejecta haloes are present for craters of Lower Imbrian age and younger (Ghent et al., 2005). These haloes appear farther from the crater rim than blocky proximal continuous ejecta, which show brighter than average radar returns. Radar-dark haloes are not detectable in visible-wavelength images. Unlike spectral reflectance measurements, radar observations use long-wavelength signals that penetrate up to tens of meters, and thus return information representing a larger integrated volume of regolith. Here we use Earth-based radar images acquired using the 430 MHz (70-cm wavelength) and 2380 MHz (12.6-cm

* Corresponding author.
E-mail address: ghentr@geology.utoronto.ca (R.R. Ghent).

0019-1035/$ - see front matter © 2010 Elsevier Inc. All rights reserved.
doi:10.1016/j.icarus.2010.05.005

wavelength) transmitters at the Arecibo Observatory radio telescope, and receivers at the Green Bank Telescope in West Virginia (Campbell et al., 2007). At both wavelengths, we transmit circularly polarized radar signals and receive echoes in the same (SC) and opposite (OC) senses of circular polarization. The OC signal comprises specular reflections and a component of diffuse echoes from wavelength-scale features, whereas SC echoes are primarily sensitive to diffuse scattering on and within the regolith. The ratio of SC to OC echoes, termed the circular polarization ratio (CPR), provides enhanced sensitivity to scattering from blocks suspended in the upper several meters of the regolith. In 70-cm wavelength images, radar-dark haloes show low OC and SC returns and low CPR values, indicating depletion in blocks or boulders capable of scattering the incident energy – i.e., blocks about 1/10 the wavelength or larger in diameter (7 cm) – within the radar penetration depth (Ghent et al., 2005, 2008; Thompson et al., 2006). Fig. 1 shows 70-cm (left) and 12.6-cm (right) mosaics of regions surrounding craters Aristoteles (a–c) and Aristarchus (d); (a) and (b) are OC and CPR images, respectively, and (c) and (d) show CPR in color overlain on OC images. Topographic features, such as crater rims, are most easily distinguished in OC mosaics, because OC returns are dominated by specular reflections. Close to the crater rims, blocky ejecta appear as radar-bright annuli (delineated in Fig. 1b), showing high OC and SC returns and high CPR values.

Radar-dark, block-poor ejecta haloes are emphasized in CPR mosaics (Fig. 1b–d). In general, we observe little correspondence between the presence or character of radar-dark haloes and lithological variations (Ghent et al., 2005; Thompson et al., 2006). The halo surrounding the 40-km diameter crater Aristarchus illustrates this well (Fig. 1d). The crater straddles the large fault that bounds the Aristarchus plateau, and its ejecta juxtapose rocks of markedly different lithologies (Guest and Spudis, 1985; Lucey et al., 1986). Aristarchus' radar-dark halo, however, does not vary in echo strength, morphology, or radial extent between the portions of the ejecta blanket dominated by mare versus highlands debris. Similarly, other radar-dark haloes that straddle highland-mare boundaries (e.g., Aristoteles; Fig. 1a–c) lack variations in radar echo strength or morphology corresponding to the underlying lithological boundaries, and the population of mare haloes is indistinguishable in extent and character from the population of haloes in the highlands.

New radar images at 12.6-cm wavelength with 80-m spatial resolution provide an independent observation of halo morphology and extent. Comparison of images at these two wavelengths allows more detailed examination of the nature of ejecta within the bright and dark haloes, and of the transitions from radar-bright to radar-dark at the outer bright halo edges and from radar-dark to background regolith at the outer dark halo edges. We observe that at 70-cm wavelength, the transition from bright to dark appears quite sharp (e.g., Fig. 1b); at 12.6 cm, this boundary commonly appears farther from the rim, is more gradational, and shows more fine detail (e.g., Fig. 1d; compare left and right panels). In addition to the higher spatial resolution of the 12.6-cm observations, this difference arises because the 12.6-cm radar is sensitive to smaller scatterers than the 70-cm radar ($d \geqslant 1$ cm vs. $d \geqslant 7$ cm, respectively); furthermore, the 12.6 cm returns originate within the top ~1 m of regolith, whereas 70-cm signals penetrate to ~7 m. Thus, as the proximal ejecta blanket thins with distance from the crater rim, and becomes dominated by smaller rocks, it ceases to be bright at 70 cm but remains bright at 12.6 cm.

By contrast, the distal boundaries of radar-dark haloes mapped at 12.6 cm are quite sharp, and coincide with those mapped at 70-cm wavelength (Fig. 1). This indicates that the rock-poor ejecta deposits are at least as thick as the penetration depth of the 70-cm signals (~7 m), and sufficiently fine-grained to produce low echoes and CPR at 12.6 cm (i.e., depleted in particles on the order of 1 cm and larger). Based on this new observation, we can now conclude that the lunar radar-dark halo material forms a thick, uniform mantling layer that maintains a finite thickness to its outer edge. Though emplacement of even fine ejecta at high velocity is likely to cause significant disruption of the pre-existing surface, the radar-dark haloes do not simply result from disturbance of the pre-existing regolith by large ejecta, because the haloes' observed radar signature requires a volume of fine material sufficient to cover blocks that would lead to high radar backscatter. Consistent with this idea is the fact that the fine material has retained its characteristic radar signature for up to 3 billion years (in the case of the oldest examples), indicating a thickness sufficient to survive impact overturn and homogenization – on the order of meters, rather than centimeters (Gault et al., 1974).

2.2. Radar-dark haloes on Venus

Radar-dark extended ejecta deposits are also known for Venus from 12.6-cm wavelength Magellan radar images. We focus here on large, quasi-circular radar-dark haloes (e.g., Schaber et al., 1992) of similar morphology to the lunar examples (Fig. 2), rather than the westward-opening radar-dark parabolas, which likely result from entrainment of fine-grained ejecta in prevailing high-altitude winds (Campbell et al., 1992; Schultz, 1992b). Venusian halo margins, like those on the Moon, are generally sharp and well defined. In places, haloes are contained by ridges or other topographically high features (Fig. 2). Though polarimetric information is not available for Magellan observations, the fact that the venusian haloes appear dark at 12.6 cm suggests that they have a minimum average thickness on the order of 1 m. Earth-based polarimetric S-band radar images show an enhanced degree of linear polarization associated with some venusian crater halos, consistent with penetration of the radar wave into a fine-grained mantling layer. Atmospheric drag should cause additional comminution of already-shocked material (Schultz, 1992b), so it is likely that radar-dark haloes on Venus are characterized by smaller particles than those on the Moon, for a given crater size.

2.3. Low nighttime temperature haloes on Mars

Using the global mosaic of THEMIS nighttime IR data from JMARS (Christensen et al., 2007) and Viking, THEMIS VIS and MRO CTX images, we investigate martian craters with haloes that show low nighttime temperatures, suggesting the presence of small, unconsolidated particles. These low-temperature haloes commonly show radial texture in the form of wisps or streaks of relatively cool nighttime temperature material; some show feathery margins with individual streaks that extend many crater radii from the center, whereas others have smooth, well-defined margins and circular planforms. Three examples are shown in Figs. 3–5. Low-temperature haloes occur in association with craters that span the range of ejecta morphology classifications designated by Barlow et al. (2000) and Barlow (2005). Some haloes coincide over parts of their margins with outer layered ejecta lobes or other extended ejecta deposits; however, for most of the low-T halo margins, particularly those with digitate or wispy edges, at least part of the low-temperature material lies well outside the outer ejecta lobes or run-out features.

Other studies have detailed the morphology, morphometry, and thermal properties of various types of layered ejecta on Mars, associating variations in grain size with various ejecta facies. For instance, Baratoux et al. (2005) examined variations in nighttime temperatures at the edges of lobate ejecta in Syrtis Major, attributing the temperature anomalies to variations in particle sizes at lobe termini, likely caused by kinematic sieving during ejecta emplacement. Boyce and Mouginis-Mark (2006) specifically examined dou-

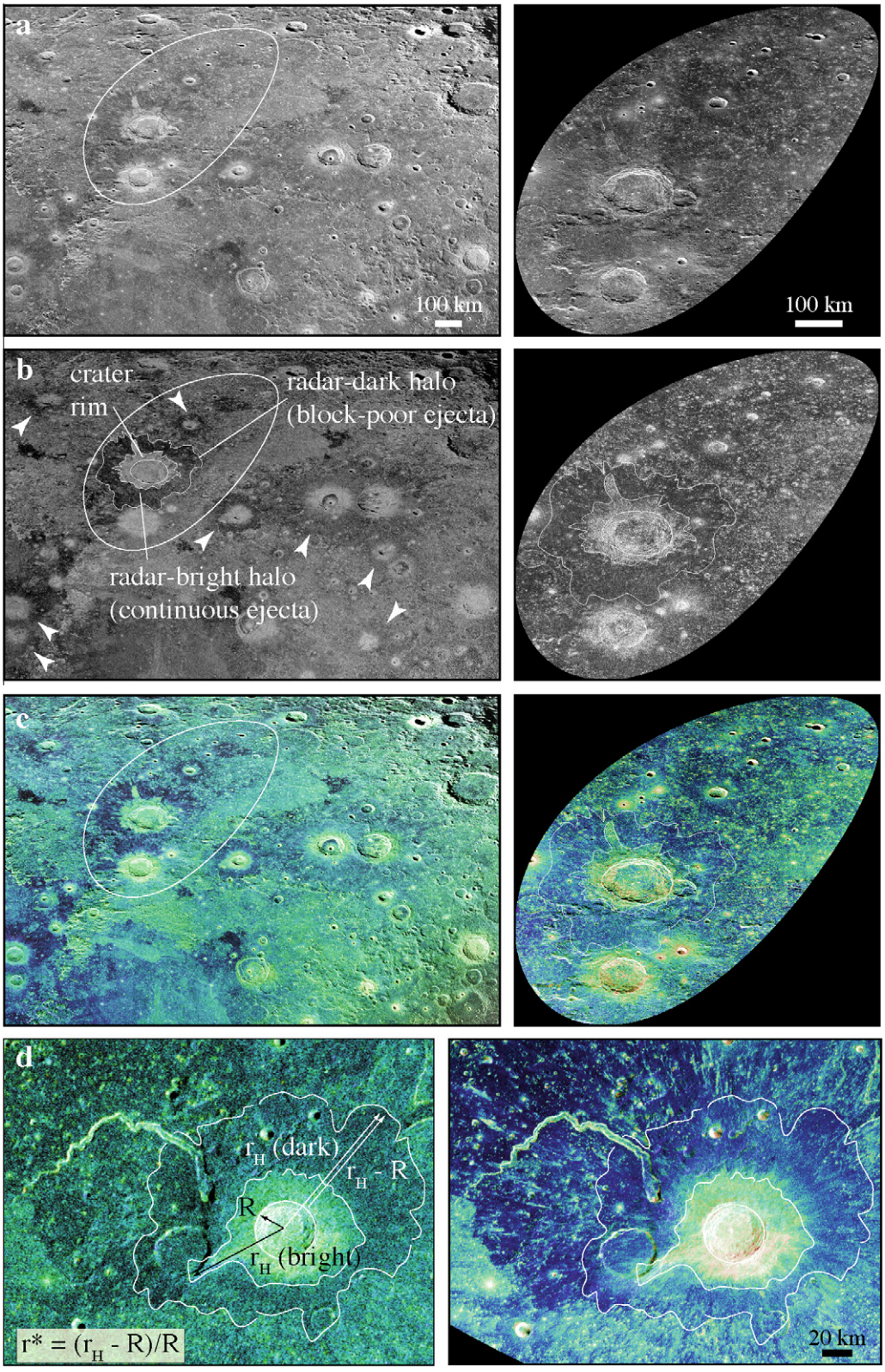

Fig. 1. (a–c) Earth-based radar mosaics of lunar craters Aristoteles (50.2°N, 17.4°E, d = 87 km) and (d) Aristarchus (23.7°N, 47.4°W, d = 40 km). In all frames, left: 70-cm mosaic, 400 m/pixel spatial resolution; right: 12.6-cm mosaic, 80 m/pixel spatial resolution. (a) OC mosaics; (b) CPR mosaics showing outlines of bright and dark haloes as observed in 70-cm images; white arrows mark other craters with radar-dark haloes; (c) CPR as color overlay on OC radar image; outlines as in (b); and (c) CPR as color overlay on OC image; outlines as in (b); R, r_H, and r^* are shown. Note that 12.6-cm bright halo extends beyond 70-cm bright halo, while 12.6- and 70-cm dark haloes are coincident.

ble layered ejecta (DLE) deposits and concluded that different mechanisms were responsible for emplacing the inner versus outer ejecta layers. They observed that the outer layers are commonly characterized by a distinct radial fabric that in places flows around or over low-relief obstacles, indicating relatively slow motion along the ground. In addition, they noted thin radial wisps

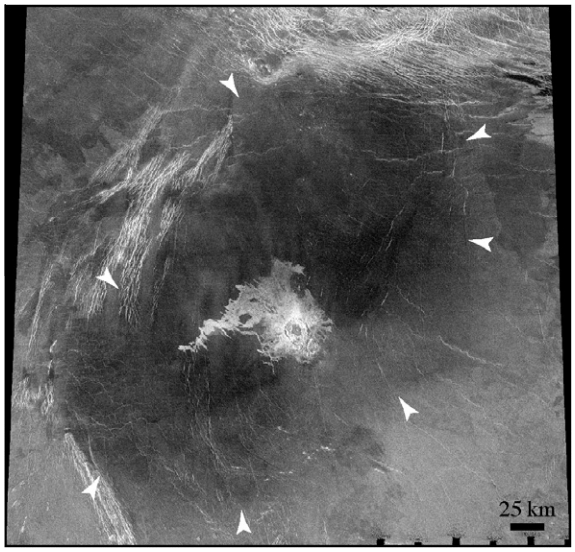

Fig. 2. Magellan left-look radar image of venusian crater Galina (47.6°N, 307.1°E, d = 16.8 km). White arrows denote distal margins of radar-dark halo.

extending beyond the limits of ejecta lobes, and they documented a number of observations indicating a very thin (on the order of 10 m) erodable facies distal to the outer ejecta layer margins. These observations are generally consistent with those presented in this paper. However, we observe low-T haloes for craters with a range of ejecta morphologies, indicating that emplacement of low nighttime temperature materials is not restricted to DLE craters. Komatsu et al. (2007) examined a number of different types of layered ejecta structures and observed that the outer layers are sometimes cooler at night than inner layers. Though all of these studies observe morphological characteristics that suggest particle size variations within ejecta deposits, none has specifically examined the low-T haloes described here. Because these low-T haloes occur for craters with a range of ejecta morphologies, and because they commonly extend beyond the maximum run-out distance for any of those ejecta, we conclude that low-T haloes are distinct from other types of layered ejecta, and that their emplacement is ubiquitous under certain conditions.

The low nighttime temperatures exhibited by the martian haloes suggest small particle sizes. To quantify this, we use thermal inertia calculated from THEMIS to exploit the measured relationship between thermal conductivity and particle size under martian atmospheric conditions (Presley and Christensen, 1997). In terms of thermal inertia, I, we have:

$$d = \left(I^2/(\rho c) * 1/\left(CP^{0.6}\right)\right)^{-1/(0.11\log P/K)} \quad (1)$$

where d = particle diameter, C = 0.0015, $K = 8.1 \times 10^4$ torr, P = atmospheric pressure (torr), and where we use the canonical value $\rho c = 1 \times 10^6$ J/m^3 K. The atmospheric pressure varies with topographic elevation as

$$P = P_0 e^{-h/\tau} \quad (2)$$

where P_0 = 4.6 torr and τ = atmospheric scale height (taken as 10.8 km at 210 K, Presley and Christensen, 1997). For intermediate values of thermal inertia, particle sizes calculated in this way are non-unique, because unlike for cases of very low or very high values of thermal inertia (arising from dust or exposed rock, respectively), there are a number of different combinations of particle types and sizes that could lead to a given intermediate thermal inertia value. Furthermore, the thermal conductivity measurements reported in Presley and Christensen (1997) were performed on assemblages of spherical particles of uniform size; even highly comminuted crater ejecta are not likely to be comprised of purely unimodal particle size distributions. However, Presley and Craddock (2006) measured thermal conductivities for non-uniform particle assemblages, and found that the aggregate conductivity of such an assemblage is dominated by the largest particles present; thus, particle sizes calculated using the method of Presley and Christensen (1997) can at least place bounds on the maximum particle size represented in a given sample. Given these caveats, we find, using thermal inertia values (ranging from 64 to 486) calculated from THEMIS data for selected craters (Fergason et al., 2006), that the particles represented in the martian haloes to range from <10 μm to ~10 mm in diameter.

3. Fine ejecta run-out

Given the availability of a full nearside radar dataset for the Moon at 70 cm, a growing database of radar images at 12.6 cm, and nearly global coverage of THEMIS nighttime IR images for Mars and Magellan radar images for Venus, we undertook a survey of the crater size-scaled maximum run-out exhibited by all fine-ejecta haloes for craters with $d > 5$ km on the Moon and Venus, and $d > 2$ km on Mars. Measurements of maximum ejecta run-out provide valuable constraints on the emplacement process. For the fine ejecta on which we report here, the differences between the scaling of lunar haloes and those on Mars and Venus provide an opportunity to isolate atmospheric effects. Furthermore, comparison between our observations (which constitute the first systematic study of ejecta scaling using large sample sizes) and predictions based on theoretical and experimental work highlight shortcomings in current understanding of ejecta emplacement processes.

For the Moon, we identified radar-dark haloes using OC, SC, and CPR images at 70-cm wavelength; for Mars, we used THEMIS day- and nighttime thermal IR global mosaics. For both the Moon and Mars, we digitized crater rims and halo outlines manually from the images using ArcGIS; we then calculated the geographic coordinates of the crater centroid, the crater radius (R), and the distance from the centroid to each halo vertex. We define the halo radius (r_H) as the distance from the crater centroid to the most distant halo vertex (Fig. 1b), and ejecta run-out r^* (Fig. 1b) as:

$$r^* = (r_H - R)/R \quad (3)$$

following the convention of Schultz (1992a). Finally, we regressed $\log(r^*)$ against $\log(R)$, and we report the results with 95% confidence intervals on the regressions (Fig. 4).

For Venus, we adopted crater radii and geographic centroid locations from the Herrick et al. (1997) crater database; we digitized halo outlines using Magellan radar images and calculated r_H, r^*, and the regressions for radar-dark haloes using the same method as for the Moon and for Mars.

Log–log regressions of r^* vs. R for 200 lunar radar-bright haloes and 275 lunar radar-dark haloes (Table 1), 196 venusian radar-dark haloes (Table 2), and 88 low-temperature martian haloes (Table 3) are shown in Fig. 6. For all three planets, ejecta haloes scale with crater radius according to a power-law relationship:

$$r^* = aR^b \quad (4)$$

3.1. Lunar bright haloes

Lunar radar-bright haloes scale with crater radius according to Eq. (4), with a = 1.1 and b = −0.008. This relationship is very close to that reported from measurements on photographs of lunar continuous ejecta (e.g., Moore et al., 1974; Gault et al., 1975). Further, the commonly used scaling of McGetchin et al. (1973), derived using empirical observations of terrestrial explosion and impact

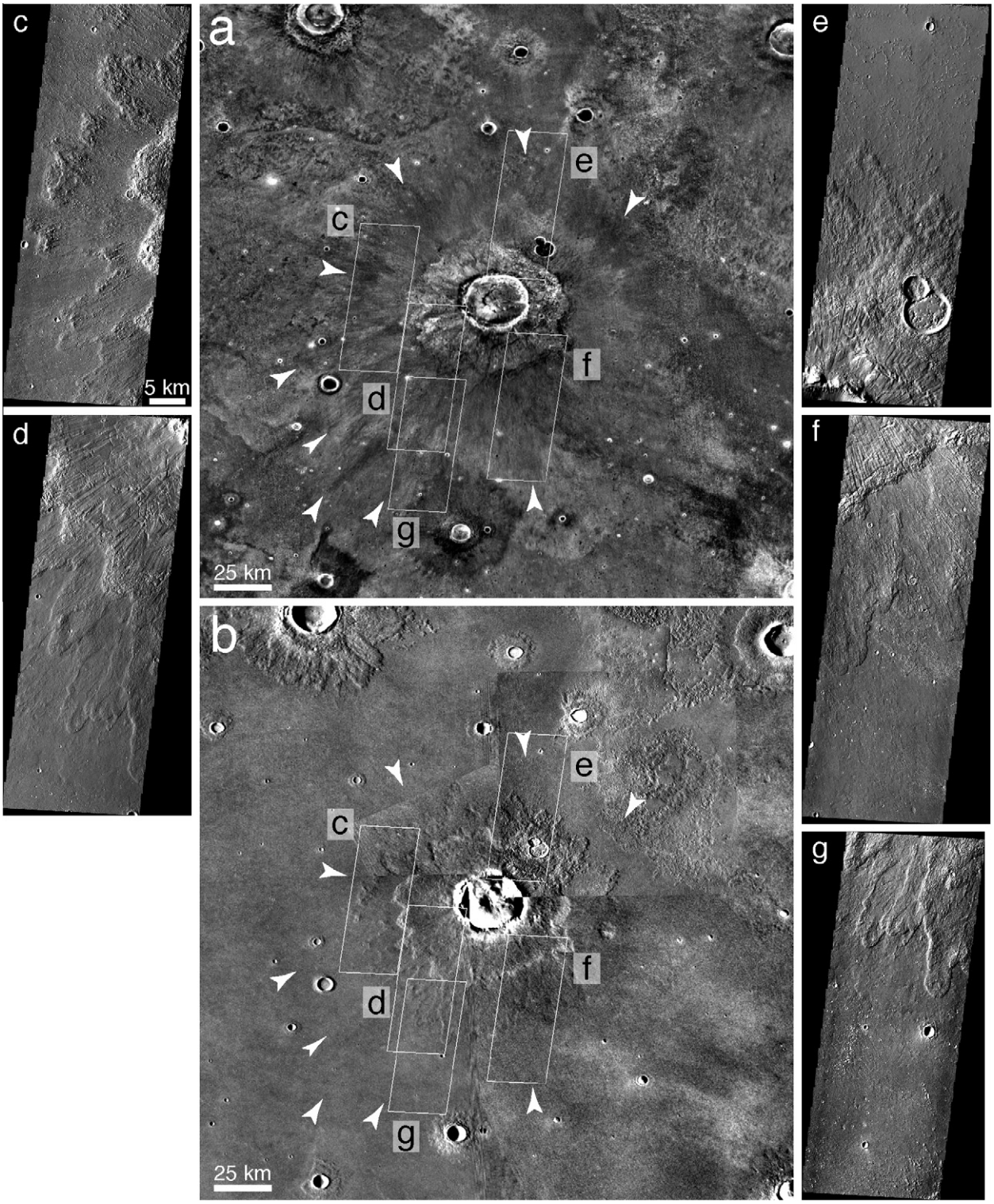

Fig. 3. Martian crater Bacolor (32.97°N, 118.65°E, d = 22.8 km), designated as a DLE crater in Barlow (2005). (a) Portion of THEMIS nighttime IR global mosaic; (b) portion of Viking MDIM 2.1 global mosaic; (c–g) portions of THEMIS VIS images, all 18 m/pixel and shown at the same scale: (c) V05114012; (d) V13988002; (e) V13364007; (f) V11829005; (g) V28851009. White arrowheads in (a and b) denote margins of low-temperature halo. Inner and outer ejecta lobes are clearly visible in (b–f), but no materials corresponding to the margins of low-temperature halo are apparent in either the Viking or THEMIS VIS images. The smaller crater near the box denoting image g also shows a low-temperature halo that similarly does not appear in the visible-wavelength images (b and g).

craters and estimates of the thicknesses (t) of lunar impact ejecta blankets, predicts that continuous ejecta should thin with distance r from the crater rim as

$$t \sim R_t^{0.74}(r/R_t)^{-3} \quad (5)$$

where R_t is the transient crater radius. If we assume that our radar-bright lunar ejecta blankets have uniform thickness at their outer edges (equal to the minimum thickness of blocky material required to produce a bright signature at 70 cm), we can recast Eq. (5)

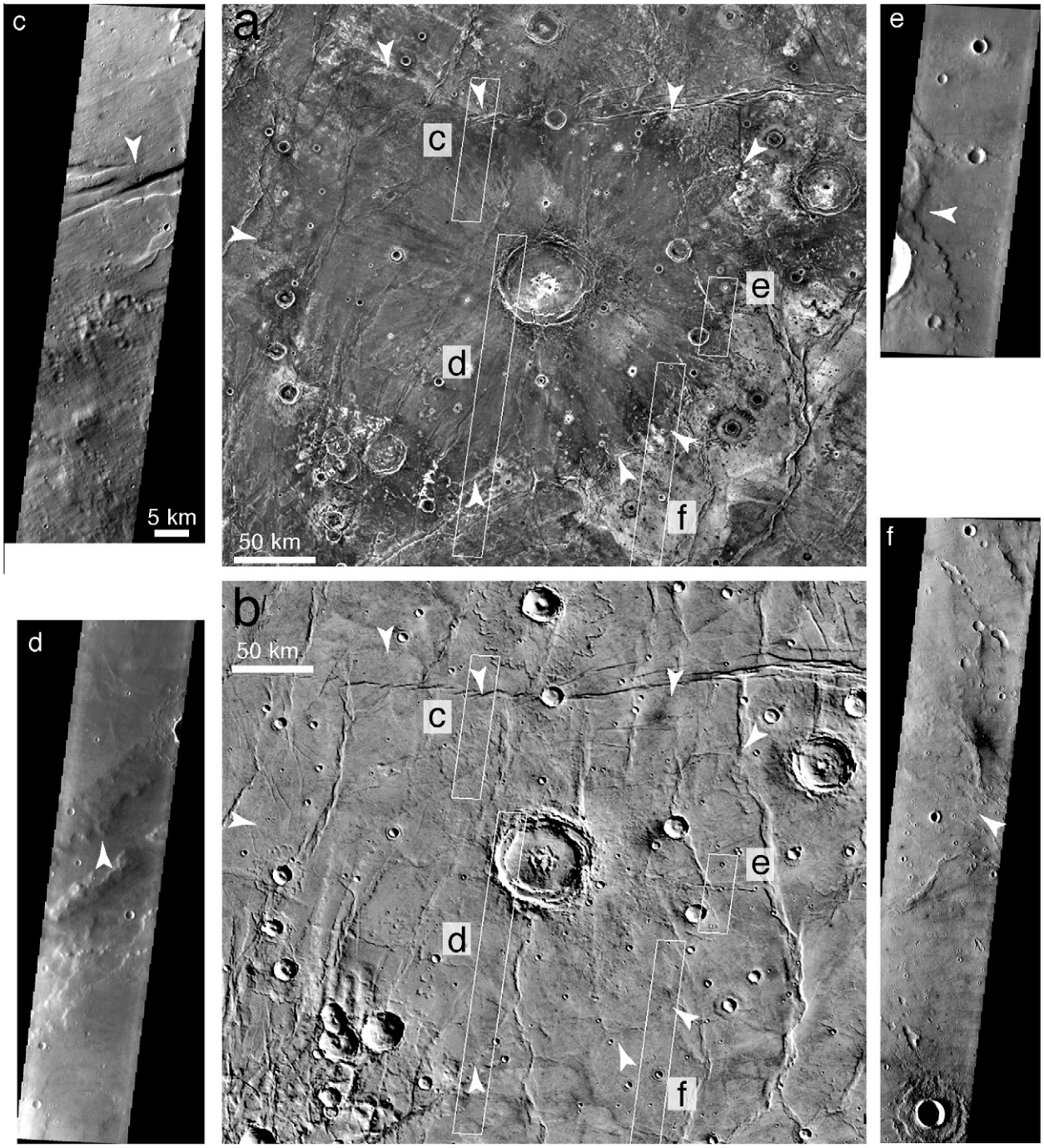

Fig. 4. Martian crater Martin (21.39°S, −69.22°E, d = 60.5 km), designated as an MLE crater in Barlow (2005). (a) Portion of THEMIS nighttime IR global mosaic; (b) portion of Viking MDIM 2.1 global mosaic; (c–f) portions of THEMIS VIS images, shown at the same scale: (c) V27573004, at 35 m/pixel; (d) V22756005, at 34 m/pixel; (e) V23305004, at 17 m/pixel; (f) V31266005, at 35 m/pixel. White arrowheads in (a and b) denote margins of low-temperature halo. Ejecta lobes are visible near the crater rim in (a and b), but the margins of the low-temperature halo lie well outside them.

$$r_H \sim R_t^{1.25} \tag{6}$$

where r_H is halo radius (Thompson et al., 2006; Ghent et al., 2008). For large craters, post-impact collapse and mass wasting enlarge the crater cavity, such that the final radius R can be significantly larger than the transient radius R_t therefore, we estimate transient crater diameters from final crater diameters using the expression (Melosh, 1989):

$$D_t^3 H_t = \frac{5D^3 H}{1 + 6[1 + D_f/D + (D_f/D)^2]^{-1}} \tag{7}$$

where D_t = transient crater diameter; H_t = transient crater depth; D = final rim-to-rim diameter; H = final depth; and D_f = final floor diameter. We use the relationships between H and D, and between D_f and D, measured for lunar craters by Pike (1977), and assume that $H_t/D_t = 1/2.7$ (Melosh, 1989). Finally, regressing r_H against R_t for the radar-bright haloes yields

$$r_H = 1.5\ R_t^{1.25} \tag{8}$$

in agreement with the McGetchin et al. (1973) prediction. Because the lunar radar-bright haloes are ejected and emplaced ballistically,

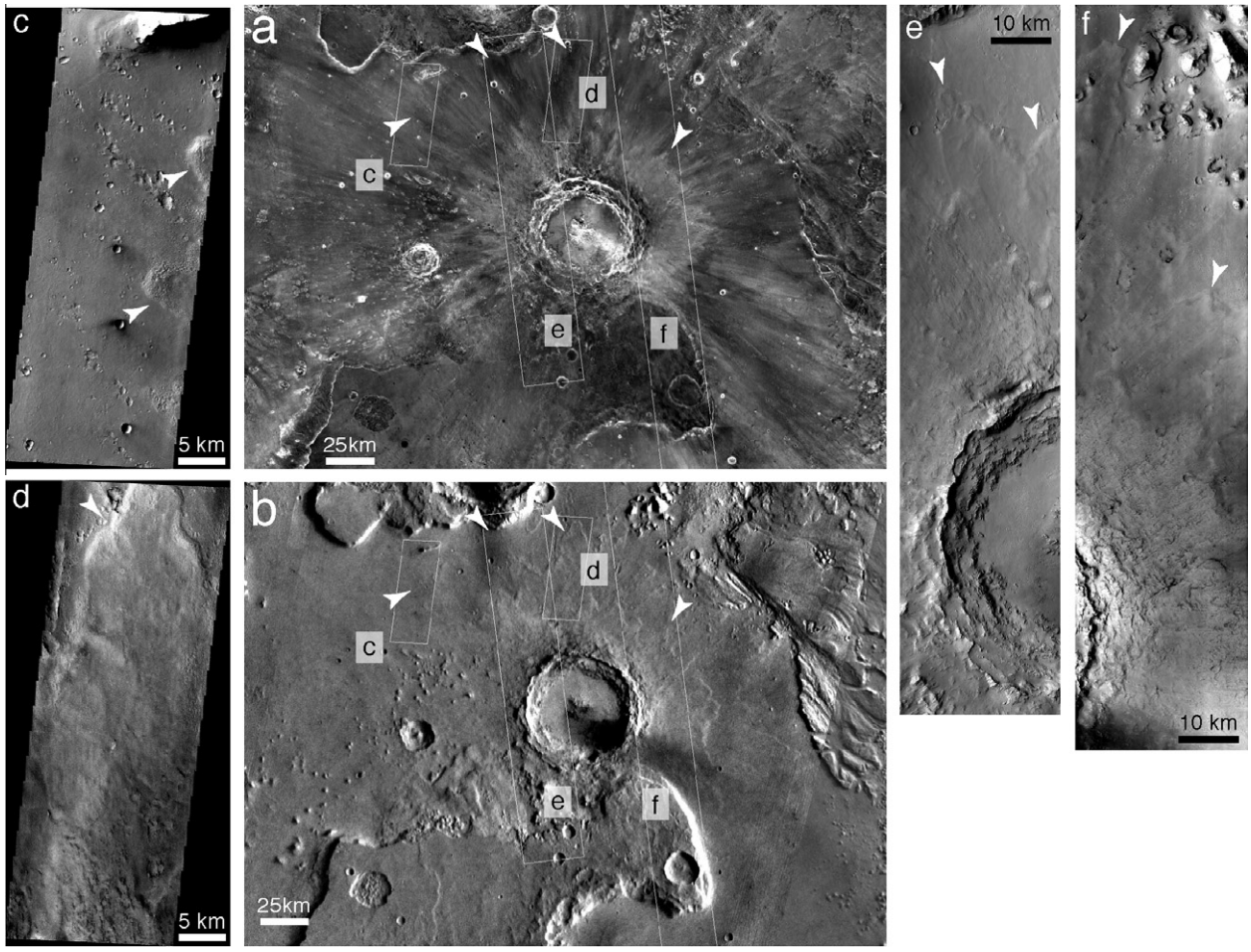

Fig. 5. Martian crater Mojave (7.45°N, −32.96°E, d = 63.14 km), given no ejecta classification by Barlow (2005); listed as MLE in the "Revised Catalog of Large Martian Impact Craters" (Barlow, personal communication, 2010). (a) Portion of THEMIS nighttime IR global mosaic; (b) portion of Viking MDIM 2.1 global mosaic; (c) portion of THEMIS VIS image V28669053, at 18 m/pixel; (d) portion of THEMIS VIS image V17450024, at 18 m/pixel; (e) portion of CTX image P03_002167_1877_XI_07N033 W, full resolution at 6 m/pixel; and (f) portion of CTX image P13_005925_1877_XN_07N032 W, full resolution at 5.5 m/pixel. White arrowheads in (a and b) denote margins of low-temperature halo; arrows in inset images (c–f) show corresponding features. The northern half of the low-temperature halo corresponds somewhat closely with ejecta lobes visible in Viking, THEMIS VIS, and CTX images, though fine structure in the low-temperature material appears as streaks well outside these lobes to the NW, W, and SE.

we can use them as a basis for comparison with emplacement in the presence of an atmosphere.

3.2. Lunar dark haloes

Lunar radar-dark haloes scale with crater radius similarly to the lunar bright haloes ($r^* = 5.9\ R^{-0.18}$), but the slope of the regression falls off more quickly with increasing crater size. The final ejecta run-out is the sum of the ballistic range and subsequent motion along the ground surface, which is proportional to the ejection velocity (and therefore inversely proportional to ejecta mass). Large ejecta travel farther along the ground, relative to crater size, than do small ejecta; thus, r^* falls off more quickly with crater size for fine ejecta (dark haloes) than for coarse ejecta (bright haloes). The radial extent of lunar ejecta of a given size, no matter how small, therefore constrains the range of ejection velocities produced in a given impact.

The large radial extent of fine-grained ejecta haloes suggests that they represent a volumetrically significant contribution of fine material to the regolith, though no reliable constraints on halo thickness have thus far been available. The coincidence reported here of lunar halo margins as imaged at 12.6-cm and 70-cm radar wavelengths indicates that the lunar haloes are everywhere thick enough to produce dark returns at 70-cm wavelength, or at least ~7 m. It is likely that the depth of fine halo-forming ejecta increases as a function of r/R (range from crater center, normalized to crater radius) toward the crater rim; lacking an independent constraint on this function, we can estimate a lower bound on halo volume by assuming a uniform thickness of 7 m and integrating over the annulus between crater rim and halo margin. Incidentally, for craters with prominent radar-bright continuous ejecta blankets, we cannot determine from radar images whether or not fine ejecta extend beneath, on top of, or among the radar-bright blocky ejecta all the way from the crater rims to the outer halo margins. However, we have mapped 75 small craters that have radar-dark haloes but no radar-bright haloes at 70-cm wavelength, suggesting that fine material comprises part of the near-rim ejecta for all lunar craters.

We find that halo volumes normalized to transient crater volumes, V_t (assuming parabolic transient craters with volume $pH_tD_t^2/8$) follow an inverse power-law scaling with transient crater radius (Fig. 7), with an exponent opposite in sign but approximately equal in magnitude to that estimated for normalized impact melt volumes (Cintala and Grieve, 1998). Absolute halo volumes range from 0.669 to 0.006 V_t for craters with final radius R = 3.7–320 km (Orientale ring 2), respectively, representing a range of 3.4 km^3 to 2.3×10^4 km^3. For comparison, estimated melt volumes are 0.4 km^3 (0.006 V_t) and 7.1×10^5 km^3 (0.177 V_t), respectively, for the same two craters.

Table 1
Locations and sizes of lunar craters with haloes in 70-cm wavelength Earth-based radar images.

Name	Latitude (°)	Longitude (°E)	Crater radius (km)	Dark halo radius (km)	Bright halo radius (km)[a]
Angstrom	29.9	318.6	5.0	30.0	8.6
Aratus	23.4	4.6	5.9	37.2	20.3
Archytas	58.6	5.2	17.3	85.8	34.4
Aristarchus	23.7	312.7	20.5	123.3	51.4
Aristillus	33.7	1.3	28.0	131.9	88.1
Aristoteles	50.1	17.4	47.5	156.6	121.5
Artsimovich	27.6	323.6	4.7	29.2	n/a
Atlas	46.6	44.4	46.9	204.9	94.2
Autolycus	30.5	1.7	21.4	95.6	64.0
Bancroft	28.0	353.7	7.0	41.2	21.7
Bessel	21.7	17.9	10.2	53.9	16.3
Borel	22.4	26.4	3.5	18.3	n/a
Bullialdus	−20.7	337.7	32.4	111.0	56.8
Burg	44.9	28.2	20.1	92.5	59.0
Byrgius D	−23.9	293.0	13.7	71.2	24.9
C. Herschel	34.4	328.9	7.1	55.3	12.9
Cardanus	13.3	287.9	27.2	137.9	39.3
Carlini	33.7	336.1	5.3	66.0	n/a
Cauchy	9.4	38.6	7.2	46.8	14.5
Cavalerius	5.1	293.3	33.1	125.9	58.9
Cepheus	40.6	45.6	21.4	85.8	42.8
Copernicus	9.6	340.1	49.7	188.0	120.5
Daniell	35.3	31.1	14.3	48.8	n/a
Dawes	17.1	26.4	11.2	53.8	24.2
Delisle	29.9	325.5	13.6	79.7	26.4
Diophantus	27.6	325.9	9.3	61.1	19.7
Eichstadt	−22.4	281.9	29.5	92.6	62.9
Encke	4.6	323.5	14.9	63.2	24.2
Euclides	−7.4	330.6	10.4	63.1	19.8
Eudoxus	44.0	16.4	37.0	150.5	98.0
Fabricius	−42.7	41.6	41.3	153.0	94.4
Franklin	38.7	47.6	30.4	92.2	49.0
Galilaei	10.5	297.4	8.4	49.9	13.3
Galilaei A	11.7	297.2	6.1	30.0	11.8
Galle	55.7	22.4	11.4	62.2	20.7
Gruithuisen	32.8	320.5	8.6	44.7	23.0
Harpalus	52.6	317.0	21.7	82.6	46.0
Hell	−32.3	352.2	17.5	120.1	47.1
Henri Freres	−23.5	301.3	22.4	100.8	64.5
Hercules	46.6	39.1	37.2	211.2	112.6
Herigonius	−13.3	326.2	10.1	35.0	13.5
Kirch	39.2	354.5	6.3	25.6	11.4
Krafft	16.6	287.6	26.4	87.2	42.9
Lambert	25.7	339.2	16.3	57.1	n/a
Langrenus	−8.7	60.9	65.1	263.0	193.8
Le Verrier	40.2	339.6	10.8	45.2	23.0
Lichtenberg	31.9	292.6	10.4	35.9	17.8
Luther	33.1	24.1	6.4	32.6	n/a
Maestlin	4.9	319.5	3.7	30.7	8.3
Mairan	41.4	316.8	20.7	115.7	40.8
Manilius	14.3	9.1	20.8	70.3	43.1
Markov	53.3	297.8	21.0	97.5	n/a
Nielsen	31.8	308.5	5.1	36.2	n/a
Norman	−11.7	329.8	6.1	37.9	n/a
Orientale (ring 2)	−19.5	268.0	320.0	1066.0	n/a
Peek	2.6	86.7	8.0	36.8	n/a
Peirce	18.2	53.2	9.7	38.1	11.5
Petavius	−25.1	60.3	91.0	295.1	165.5
Petavius B	−19.8	56.8	18.4	103.5	62.3
Piazzi-Smyth	41.7	356.9	7.5	28.5	13.1
Picard	14.6	54.6	11.5	43.0	21.7
Piccolomini	−29.6	32.1	49.4	147.7	79.1
Plato	51.4	351.0	54.7	220.0	121.9
Plinius	15.2	23.6	23.1	80.1	40.0
Pytheas	20.6	339.5	10.1	75.0	18.8
Reiner	6.9	305.2	15.6	111.8	29.0
Rothmann	−30.6	27.6	23.8	90.3	50.0
Sarabhai	24.7	21.0	5.2	29.9	n/a
Schluter	−5.6	276.9	45.6	176.5	92.3
Sinus Iridum	44.1	328.5	118.0	856.0	n/a
Stevinus	−32.4	53.9	38.0	144.3	118.6
Sulpicius Gallus	19.6	11.7	7.6	32.5	12.6
Taruntius	5.5	46.5	29.3	101.0	56.4
Theaetetus	36.8	6.2	13.4	92.8	45.8

(*continued on next page*)

Table 1 (*continued*)

Name	Latitude (°)	Longitude (°E)	Crater radius (km)	Dark halo radius (km)	Bright halo radius (km)[a]
Theophilus	−11.3	25.1	55.9	216.6	95.1
Timocharis	26.7	347.0	17.6	86.5	39.7
Tycho	−43.1	348.8	44.5	336.8	189.1
Werner	−27.8	3.2	38.0	145.2	69.1
Wichmann	−7.5	322.1	5.9	26.0	13.6
Wollaston	30.6	313.3	5.2	24.7	n/a
Zucchius	−61.4	309.8	35.6	153.9	152.0
	32.3	14.0	3.7	27.2	5.6
	60.3	332.7	4.0	16.0	6.4
	−24.0	319.4	3.0	21.5	6.4
	47.1	353.5	2.9	20.4	6.4
	42.8	292.9	3.7	17.3	6.6
	42.3	343.2	3.7	13.0	6.6
	37.1	327.7	4.9	24.0	6.8
	40.8	309.5	3.4	33.0	7.0
	−29.1	324.3	4.6	16.6	7.5
	22.4	57.5	4.0	30.3	7.6
	−25.7	323.9	4.3	24.8	7.7
	40.4	23.6	3.2	24.3	7.7
	37.0	25.9	3.4	22.1	7.8
	56.1	316.8	4.2	16.1	7.8
	−48.0	313.2	4.8	26.8	8.0
	49.6	344.1	3.8	24.5	8.0
	−23.8	327.2	4.7	16.9	8.2
	39.7	24.0	2.8	19.3	8.3
	50.4	9.1	4.4	27.2	8.8
	42.9	349.9	5.4	17.6	8.8
	38.6	303.3	3.9	28.6	8.8
	55.5	315.3	5.8	40.9	9.2
	−16.5	336.5	4.5	22.1	9.2
	0.2	329.0	5.0	28.0	9.2
	−21.6	323.1	5.6	24.3	9.4
	22.5	56.8	6.6	25.5	9.5
	9.3	328.1	4.9	36.8	9.8
	10.0	318.3	6.5	39.0	9.8
	37.4	299.8	5.3	28.7	10.1
	32.9	344.2	4.6	21.1	10.3
	0.7	323.7	5.4	26.3	10.3
	47.1	334.8	6.0	31.4	10.5
	−9.2	314.1	4.6	40.6	10.6
	−57.3	4.6	5.2	37.9	10.7
	49.5	345.7	5.4	16.5	10.8
	−51.4	55.8	5.1	48.1	10.9
	−27.2	342.4	6.7	31.9	11.2
	−40.9	301.6	8.0	33.4	11.2
	−62.0	11.3	6.9	42.6	11.6
	−22.0	347.5	8.8	37.3	12.1
	−5.4	313.9	6.3	54.0	12.2
	46.4	344.8	6.7	26.9	12.6
	27.7	49.3	5.3	33.9	12.6
	−21.9	325.0	5.6	27.2	12.6
	14.9	322.9	5.8	34.6	13.0
	−0.7	297.5	6.4	36.8	13.2
	−43.2	329.9	8.5	44.6	13.5
	−37.4	10.9	5.9	50.4	13.6
	−14.8	311.8	6.7	54.1	13.8
	56.8	18.2	6.2	36.4	14.0
	33.6	27.6	8.5	32.3	14.1
	−0.8	302.8	8.6	39.9	14.4
	−51.8	346.1	9.5	28.8	15.0
	−42.3	23.5	8.3	68.4	15.0
	10.0	329.9	6.8	31.7	15.3
	50.6	300.3	6.8	52.8	15.5
	−37.8	44.2	6.1	52.9	15.6
	−42.7	315.6	9.2	28.9	15.7
	−59.1	18.6	5.5	30.5	15.9
	−49.2	62.0	6.2	44.4	16.1
	−2.6	298.7	5.1	26.9	16.1
	48.9	355.6	4.4	30.2	16.3
	−42.3	19.4	8.3	42.2	16.5
	10.7	26.7	11.9	62.7	16.9
	12.6	314.2	8.2	47.6	17.3
	−55.4	26.8	8.0	44.3	17.4
	−36.6	18.3	7.8	42.9	17.7
	−34.0	27.8	7.3	48.5	17.7

Table 1 (*continued*)

Name	Latitude (°)	Longitude (°E)	Crater radius (km)	Dark halo radius (km)	Bright halo radius (km)[a]
	−53.3	27.7	9.8	44.0	17.9
	1.0	341.3	6.9	62.0	18.0
	−29.4	294.0	6.3	52.2	18.4
	51.4	10.7	6.7	47.9	18.4
	−19.7	300.0	11.7	46.8	18.8
	58.7	328.8	9.4	45.6	19.1
	−41.8	280.5	13.3	57.1	19.3
	27.3	46.9	10.2	55.6	19.6
	−36.4	9.6	7.3	51.5	19.7
	−51.3	347.3	8.7	38.7	19.7
	38.5	321.5	8.6	53.4	19.8
	−44.5	338.0	10.7	37.2	19.9
	−14.1	334.0	8.8	47.4	20.1
	−39.8	26.3	11.5	53.5	20.4
	−67.6	290.6	9.1	52.9	20.6
	−37.1	297.6	14.1	51.2	21.0
	−43.5	297.9	8.6	31.9	21.2
	−23.2	331.6	9.4	33.9	22.2
	28.2	289.4	13.4	111.7	22.3
	−47.2	64.9	7.2	50.9	23.2
	−44.1	285.7	9.6	39.7	23.4
	66.3	49.9	11.6	97.7	23.5
	−14.6	336.5	10.6	51.9	23.6
	−61.4	0.7	14.9	54.0	23.9
	43.5	288.8	12.3	51.9	24.5
	−52.3	349.9	8.5	58.4	24.5
	54.3	330.2	9.8	55.3	24.5
	19.4	40.3	10.7	56.2	24.6
	−66.8	39.8	13.9	60.7	25.5
	−54.1	53.3	14.4	61.6	25.6
	27.2	50.6	6.3	37.5	25.7
	−60.0	3.4	14.2	58.2	26.0
	35.9	41.8	11.5	44.3	26.6
	41.6	8.0	7.6	59.9	27.0
	−49.9	288.7	12.9	46.9	27.1
	−39.8	73.0	14.1	101.5	27.3
	−56.2	357.5	14.6	76.5	28.1
	−58.5	15.9	16.1	55.1	28.2
	−42.5	271.7	19.8	56.2	28.5
	−61.2	51.9	17.8	104.4	29.6
	−32.2	311.7	10.9	56.9	30.2
	−22.3	36.7	14.9	46.3	31.2
	−52.8	336.0	16.5	88.5	31.7
	−36.7	358.6	17.9	65.0	33.1
	23.3	331.0	13.5	62.1	34.8
	−16.6	293.4	23.9	115.4	35.0
	58.6	319.6	14.0	106.9	35.2
	8.1	322.2	15.5	95.3	35.8
	−43.2	8.0	14.4	88.2	35.9
	−55.1	36.7	17.5	74.0	36.9
	52.2	324.6	12.2	91.8	38.6
	61.6	50.1	16.7	94.8	38.8
	54.4	62.5	16.9	66.8	39.9
	−31.6	273.6	21.3	87.4	40.7
	62.1	35.0	21.5	82.1	41.2
	−61.6	63.9	22.6	113.7	44.1
	−44.8	278.3	32.0	122.2	44.5
	29.6	43.6	24.0	122.0	47.7
	63.1	17.5	21.3	119.0	48.4
	−66.3	53.9	22.9	145.4	51.6
	3.3	337.2	22.4	89.3	54.5
	−40.2	326.1	30.0	141.7	59.4
	34.4	56.5	47.7	175.8	76.1
	−10.4	76.0	39.7	162.3	85.4
	−65.3	271.9	95.5	477.9	135.7
	35.4	298.3	5.5	24.1	n/a
	32.7	27.1	4.3	21.0	n/a
	34.3	30.0	5.4	29.7	n/a
	29.6	21.0	4.3	24.5	n/a
	−22.6	50.9	7.2	41.5	n/a
	61.5	43.7	3.1	31.7	n/a
	65.4	41.9	8.8	51.9	n/a
	−13.7	324.5	3.4	26.1	n/a
	−13.2	330.1	6.8	41.4	n/a
	−35.5	310.1	8.7	39.9	n/a

(*continued on next page*)

Table 1 (*continued*)

Name	Latitude (°)	Longitude (°E)	Crater radius (km)	Dark halo radius (km)	Bright halo radius (km)[a]
	39.6	347.8	5.1	24.6	n/a
	35.3	333.6	3.7	24.4	n/a
	41.2	3.9	5.4	25.6	n/a
	−47.5	326.4	7.4	40.8	n/a
	−0.2	303.0	3.3	15.8	n/a
	3.1	299.3	5.0	26.4	n/a
	14.0	298.3	4.2	19.3	n/a
	23.0	298.2	4.3	20.2	n/a
	29.7	31.6	4.0	25.2	n/a
	19.7	6.4	4.1	25.0	n/a
	21.1	20.6	4.2	14.0	n/a
	17.5	33.8	11.6	36.9	n/a
	13.3	28.7	12.6	45.8	n/a
	14.1	20.3	10.1	21.4	n/a
	14.3	348.8	30.2	131.5	n/a
	−49.6	286.3	12.5	32.2	n/a
	58.9	314.6	12.5	55.9	n/a
	62.7	359.7	18.1	91.8	n/a
	−55.7	317.3	4.2	24.8	n/a
	−56.9	317.9	5.0	27.1	n/a
	−19.0	47.2	19.4	97.7	n/a
	−21.0	308.6	7.8	25.5	n/a
	51.1	43.6	16.7	53.2	n/a
	48.5	31.4	8.8	30.7	n/a
	40.2	32.9	16.1	77.8	n/a
	−56.4	54.6	5.2	20.1	n/a
	−41.4	48.0	16.5	70.9	n/a
	−25.3	306.0	14.0	48.1	n/a
	53.7	307.3	5.7	21.3	n/a
	22.6	304.8	3.5	21.6	n/a
	22.0	305.2	2.9	19.7	n/a
	21.5	308.1	5.8	21.6	n/a
	55.0	358.2	5.8	32.2	n/a
	67.4	344.4	11.2	98.9	n/a
	65.7	29.2	6.1	29.4	n/a
	67.4	35.2	6.0	25.8	n/a
	11.5	292.6	8.5	55.4	n/a
	5.2	308.7	5.4	26.2	n/a
	11.7	21.8	14.1	53.6	n/a
	11.1	23.4	3.7	13.3	n/a
	17.4	31.3	16.9	48.9	n/a
	31.3	76.7	10.3	34.5	n/a
	−19.6	306.8	10.4	40.5	n/a
	−36.5	299.1	4.7	15.9	n/a
	−48.4	312.2	9.0	28.5	n/a
	−43.6	359.4	10.8	51.8	n/a
	−36.7	13.2	8.3	32.4	n/a
	−41.3	274.1	12.9	55.2	n/a
	−51.2	51.7	4.4	15.4	n/a
	17.1	320.4	7.4	30.7	n/a
	16.1	317.6	4.8	27.8	n/a

[a] Some small craters have dark, but no bright, haloes; bright halo radii listed as n/a.

3.3. Venusian halo scaling

Unlike the lunar case, Venus' dense atmosphere has a profound effect on ejecta emplacement. Fig. 6 shows that venusian haloes are larger, for a given crater size, than lunar haloes, despite Venus' higher gravity; but r^* declines with crater size as $R^{-0.49}$. Estimates of drag on ejecta moving through the venusian atmosphere and of ejecta entrainment in vortices generated by flow separation at the upper thin edge of the ejecta curtain (Schultz, 1992a,b) lead to the prediction that $r^* \sim R^{-1/2}$ if the ejecta cloud density ρ_e is a constant fraction of the ambient atmospheric density ρ_o, or that $r^* \sim$ constant if $\rho_e \approx \rho_o$. The agreement between our observed scaling ($r^* \sim R^{-0.49}$) and the prediction for complete entrainment ($r^* \sim R^{-1/2}$) indicates that the material comprising radar-dark haloes on Venus originates in the crater cavity, and its emplacement is controlled by turbulent flow behind the outward-expanding ejecta curtain. Furthermore, this observation indicates that the density of the turbulent ejecta cloud is a constant fraction k of that of the atmosphere; additional modeling informed by our results could constrain this value.

3.4. Martian halo scaling

Following the same method as for lunar radar-dark haloes, we find a power-law relationship between r^* and R of the same form as in Eq. (4) for martian low nighttime temperature haloes. The martian haloes are, like the venusian examples, larger than lunar haloes for a given crater size (Fig. 6). This indicates a degree of entrainment either by atmospheric gases or by subsurface volatiles vaporized during impact, because the larger martian gravity would lead to shorter run-out distances on Mars than on the Moon for ballistic deposition. There are several possibilities for the mechanism of entrainment. The first is that fine ejecta are winnowed from the outward-expanding ejecta curtain by turbulent eddies originating behind the curtain (Schultz, 1992a; Barnouin-Jha and Schultz, 1996; Barnouin-Jha, 1998; Barnouin-Jha et al., 1999). This

Table 2
Locations and sizes of venusian craters with radar-dark haloes in Magellan radar images.

Name	Latitude (°)	Longitude (°E)	Crater radius (km)	Dark halo radius (km)
Abaka	−52.52	104.37	7.3	43.9
Abigail	−52.20	111.20	9.2	58.6
Adaiah	−47.28	253.35	9.0	126.0
Agrippina	−33.25	65.65	19.3	216.7
Ahava	53.56	187.30	5.2	53.6
Amalasthu	−11.51	342.41	7.7	78.4
Amaya	11.32	89.38	17.3	118.2
Anaxandra	44.24	162.27	10.2	55.7
Andreiano	−2.99	68.77	33.1	371.5
Anya	39.55	297.84	9.1	41.6
Asmik	3.96	166.41	9.8	112.7
Audrey	23.80	348.10	7.6	231.0
Avviyar	−18.02	353.67	10.3	132.3
Ayana	−29.21	175.51	6.9	46.0
Barton	27.45	337.49	26.1	178.7
Behn	−32.44	142.04	12.7	81.1
Berggolts	−63.44	53.01	14.8	61.9
Blixen	−60.13	145.69	10.4	89.7
Bonnevie	−36.13	127.04	46.1	173.0
Browning	28.28	4.93	11.7	76.4
Bryce	−62.50	196.98	12.0	83.7
Buck	−5.74	349.61	10.9	47.8
Bugoslavs	−23.00	300.42	15.0	109.3
Caccini	17.43	170.43	19.1	177.6
Callas	2.44	27.02	16.9	105.4
Christie	28.33	72.66	11.7	109.5
Cline	−21.84	317.08	19.0	234.7
Cochran	51.90	143.33	50.0	298.0
Colleen	−60.80	162.20	6.8	65.8
Comnena	1.19	343.69	9.8	222.7
d' Este	−34.26	238.93	10.8	59.4
Danilova	−26.38	337.24	24.4	191.8
Danute	−63.48	56.51	6.2	36.1
Daphne	41.31	280.38	7.8	66.4
Darline	−19.33	232.65	6.5	117.2
de Stael	37.38	324.25	12.5	220.3
De Witt	−6.53	275.63	10.4	362.0
Durant	−62.30	227.65	10.6	65.3
Duse	−82.46	357.99	15.2	159.8
Eila	−75.00	94.62	4.8	90.8
Elena	−18.34	73.37	8.8	244.3
Elizabeth	59.16	215.40	5.3	38.3
Elza	−34.42	275.89	9.0	140.7
Erin	−47.04	184.78	6.8	87.4
Erkeley	43.99	103.33	4.0	56.7
Erxleben	−50.86	39.41	15.8	171.4
Evika	−5.09	31.40	10.2	250.2
Faiga	4.92	170.91	4.8	48.1
Fazu	32.41	106.04	3.1	34.3
Felicia	−19.81	226.49	5.8	47.2
Flagstad	−54.26	18.88	19.6	164.0
Fossey	2.02	188.71	15.2	173.2
Francesca	−27.99	57.70	8.5	121.6
Gahano	−80.16	77.42	2.3	37.0
Galina	47.66	307.10	8.4	197.8
Gentilesc	45.21	260.68	10.3	68.8
Giliani	−72.92	142.12	10.0	77.5
Glaspell	−58.42	269.55	13.2	255.0
Golubkina	60.31	286.47	14.2	79.9
Grace	−13.80	268.90	9.5	73.5
Gretchen	−59.70	212.30	10.4	108.1
Halle	−19.78	145.53	10.8	192.4
Hayasi	53.78	243.87	21.6	217.3
Hellman	4.74	356.26	17.4	88.3
Hwangcini	6.30	141.76	15.1	254.9
Ichikawa	−61.57	156.32	15.7	173.0
Ilga	−12.42	307.35	5.4	126.9
Imagmi	−48.40	100.75	3.8	109.4
Ines	−67.10	241.92	5.6	77.9
Inkeri	−28.33	223.99	5.1	49.2
Istadoy	−51.79	132.60	2.7	65.9
Janina	−2.03	135.67	4.7	111.0
Jocelyn	−33.23	276.41	7.0	43.6
Juanita	−62.80	90.00	9.7	41.3

(*continued on next page*)

Table 2 (*continued*)

Name	Latitude (°)	Longitude (°E)	Crater radius (km)	Dark halo radius (km)
Kanik	−32.54	249.89	8.3	72.4
Karen	−12.40	17.70	5.3	75.6
Kastusha	−28.54	59.95	6.5	98.1
Khatun	40.33	87.19	22.1	70.2
Kitna	−28.91	277.27	7.7	179.2
Klenova	78.13	104.48	70.5	311.7
Koinyt	−30.91	293.26	5.9	87.8
Kollwitz	25.18	133.61	14.6	217.4
Kosi	−43.94	54.99	3.9	50.5
Kumba	26.30	332.70	5.7	100.9
La Fayett	70.21	107.57	19.8	120.7
Lara	−4.26	2.90	1.7	56.2
Lazarus	−52.86	127.20	12.1	65.5
Leah	−34.20	187.80	6.0	87.0
Lenore	38.70	292.19	7.8	96.5
Liliya	30.19	31.23	7.5	105.5
Lind	50.24	355.00	12.9	170.4
Liv	−21.08	303.87	5.6	79.1
Lullin	23.05	81.26	12.6	77.2
Mae	−40.50	345.20	3.8	54.9
Mansa	−33.91	63.40	4.1	111.0
Maret	−33.30	280.24	5.9	90.5
Margarita	12.70	9.20	6.5	41.9
Marysya	53.30	75.09	3.2	67.7
Masako	−30.18	53.17	11.9	215.8
Mead	12.48	57.22	135.0	489.0
Meitner	−55.59	321.60	74.5	555.5
Melanie	−62.75	144.31	6.2	51.2
Meredith	−14.52	278.88	5.7	65.5
Michelle	−19.55	40.51	7.5	467.6
Mirabeau	1.15	284.31	11.9	55.3
Mona Lisa	25.62	25.16	39.7	372.6
Montessor	59.42	279.99	21.1	118.1
Moore	−30.35	248.40	10.6	111.4
Mu Guiyin	41.19	81.02	16.2	141.1
Nadine	7.81	359.10	9.3	72.4
Ngone	6.00	331.90	6.1	110.8
Nicole	48.36	259.28	3.2	32.2
Nilanti	−38.25	331.44	4.6	80.0
Nsele	6.70	64.20	2.6	37.0
O'Connor	−25.95	143.88	15.2	186.4
Odarka	40.80	138.18	3.5	47.1
Olesya	5.61	273.30	6.0	80.6
Olya	51.41	291.79	6.7	87.3
Onissya	−25.59	150.20	4.1	67.7
Orczy	3.70	52.31	13.5	65.8
Ottavia	−47.49	187.11	6.5	129.3
Parra	20.51	78.47	21.2	91.2
Pasha	42.71	156.31	3.6	41.7
Philomena	−40.75	151.87	7.4	136.7
Polina	42.45	148.17	10.8	107.0
Pychik	−62.40	33.80	5.1	66.0
Qulzhan	23.52	165.43	4.0	152.4
Raki	−49.40	70.00	3.8	82.6
Rampyari	50.61	179.29	3.9	65.7
Regina	30.03	147.26	12.5	154.2
Ruit	72.96	334.45	3.2	80.8
Ruth	43.28	19.85	9.3	51.8
Sandel	−45.71	211.71	9.0	117.1
Sanger	33.77	288.56	41.8	198.5
Seymour	18.15	326.48	31.5	315.5
Shih Mai-Simonenko	18.45 −26.87	318.91 97.63	11.2 16.0	140.5 113.3
Sirani	−31.45	230.39	14.2	61.7
Sovadi	−44.82	225.55	6.2	115.3
Stanton	−23.26	199.27	53.5	273.5
Stefania	51.29	333.31	5.9	38.0
Storni	−9.75	245.57	10.9	131.5
Surija	5.31	178.19	7.7	82.9
Tehina	−30.36	76.42	2.7	158.6
Terhi	45.71	253.10	5.4	130.7
Thomas	−13.01	272.54	12.6	188.3
Trollope	−54.76	246.38	13.6	59.2
Udyaka	30.91	172.91	3.9	99.2
Uleken	33.72	185.10	5.5	95.8

Table 2 (*continued*)

Name	Latitude (°)	Longitude (°E)	Crater radius (km)	Dark halo radius (km)
Ulla	−51.49	184.55	5.2	57.0
Uluk	−62.20	178.59	5.2	75.5
Umkana	−53.30	198.60	3.1	46.9
Vacarescu	−62.94	199.79	15.8	71.0
Valerie	−6.37	30.95	6.8	120.7
Vallija	26.33	120.00	7.6	152.2
Vanessa	−5.98	1.89	5.0	69.3
Vashti	−6.81	43.71	8.5	390.4
Vassi	34.36	346.49	4.3	65.2
Veriko	20.41	350.10	2.6	48.0
Veta	42.61	349.49	3.2	31.9
Viola	−36.11	240.51	5.0	41.8
Virginia	−52.90	185.90	9.3	125.9
Virve	−5.06	346.90	9.0	104.1
Volkova	75.19	242.14	23.8	254.1
Von Siebo	−52.00	36.70	16.2	100.8
Weil	19.36	283.13	12.1	70.1
Wendla	22.52	207.63	2.9	27.3
Wharton	55.69	61.88	25.2	155.7
Wheatley	16.62	268.04	37.4	364.2
Wilma	36.71	1.68	6.3	60.9
Winema	3.07	168.59	10.9	82.4
Wiwi-yokp	−73.85	228.38	2.3	40.6
Xiao Hong	−43.54	101.68	19.4	230.0
Ximena	−68.21	243.62	6.4	128.8
Yale	−13.40	271.20	9.3	133.8
Yambika	32.65	208.69	3.3	58.6
Yazruk	21.19	160.23	5.2	75.2
Yetta	58.56	185.38	4.5	48.2
Yolanda	7.81	152.69	5.7	92.4
Yonok	−65.10	234.10	4.8	38.1
Yvonne	−55.99	298.40	7.3	36.3
Zenobia	−29.33	28.56	19.6	433.8
Zivile	48.84	113.12	6.8	114.1
Zuhrah	34.70	356.99	2.9	37.5
Zula	7.29	282.01	2.5	69.7
Zvereva	45.37	283.12	11.5	72.8
	43.05	150.89	1.0	22.6
	−25.26	239.89	4.0	30.1
	55.10	350.59	2.2	34.0
	47.10	6.90	2.3	38.8
	40.28	105.88	2.2	38.9
	−38.70	359.10	1.5	45.2
	35.85	164.47	1.8	46.2
	42.71	141.71	1.7	63.2
	6.35	83.35	2.3	71.6
	−27.38	330.00	1.0	81.1

process should produce crater-scaled run-out distances that increase as $R^{1/2}$ if $\rho_e \gg \rho_o$; alternatively, as for the venusian case, ejecta run-out is predicted to be independent of crater size if $\rho_e \approx \rho_o$, or to scale as $r^* \sim R^{-1/2}$ if $\rho_e \approx k\rho_o$ (Schultz, 1992a). None of these predictions matches our observed scaling: for the martian haloes, r^* decreases as $R^{-0.13}$, similar to the scaling for the ballistically emplaced lunar dark haloes. It is possible that basal shear stresses lead to vortex decay and the resulting rolloff in halo size; given the low atmospheric density on Mars, this effect should be larger on Mars than on Venus. More recent models of formation and evolution of turbulent ring vortices behind an outward-expanding ejecta curtain (Barnouin-Jha and Schultz, 1996; Barnouin-Jha, 1998; Barnouin-Jha et al., 1999) included additional phenomena not accounted for by Schultz (1992a); but calculation of the terminal behavior of the vortices, and the forces controlling the final distribution of ejecta, requires constraints on key (currently unconstrained) parameters such as ejecta effective viscosity.

High-velocity winds and entrainment of particles could also occur in association with a base surge. Here, ejecta lofted into the air fall back to the surface and run out along it, causing scouring and transporting fine particles outward (e.g., Oberbeck, 1975). This mechanism has been suggested by others to account for deposition of long run-out ejecta lobes (e.g., Boyce and Mouginis-Mark, 2006). To test the feasibility of this mechanism to produce the observed scaling, further work is required to constrain likely column heights and resulting run-out distances for the crater and particle sizes reported here.

The smallest of the particle sizes calculated above from THEMIS thermal inertia lie well within the range that could be transported by ejecta-curtain generated winds (and possibly for base-surge generated winds, as well), whereas the largest fall outside the atmospheric transport regime (Schultz, 1992a). It is possible, given the uncertainties on the calculated particle sizes, that most of the low-T halo fragments are too large to be entrained by curtain-generated vortical winds. However, expansion of an impact-generated vapor cloud resulting from direct coupling of energy to the atmosphere during the compression stage (e.g., Schultz and Gault, 1985; Schultz, 1988) can produce winds with much higher velocities. Hydrocode models of vertical impacts into a volatile-rich target under current martian conditions indicate that winds at ground level reaching several hundreds of meters per second can persist for significant lengths of time and to distances of many crater radii from the impact point (Wrobel et al., 2006). Such high-velocity winds could entrain larger particles and distribute them widely.

Table 3
Locations and sizes of martian craters with low-temperature haloes.

Name	Latitude (°)	Longitude (°E)	Crater radius (km)	Dark halo radius (km)	Ejecta[a]	Barlow (2005) crater[a]
Arandas	42.40	−14.95	13.3	95.4	ML	04SE; 292
Bacolor	32.97	118.65	11.4	94.1	DL	07SW; 40
Bamberg	39.64	−3.00	30.4	200.7	Di	04SE; 38
Bonestell	41.97	−30.31	21.5	164.8	Di	04SC; 86
Calahorra	26.45	−38.58	16.9	53.5	ML	11NW; 51
Cave	21.60	−35.59	4.7	30.1	SL	11NW; 230
Davies	45.95	0.20	25.7	138.9	Di	04SE; 307
Galap	−37.66	−167.03	2.7	31.9	No	24NW; 165
Gamboa	40.74	−44.28	18.0	106.0	DL	04SC; 73
Maricourt	53.33	−71.09	4.6	57.2	DL	03NE; 18
Martin	−21.39	−69.22	30.3	164.3	ML	18SW; 54
Mojave	7.45	−32.96	31.6	171.8	No	11SW; 365
Mut	22.35	−35.71	3.9	19.3	No	11NW; 231
Niquero	−38.80	−165.93	6.1	29.9	SL	24NW; 168
Santa Fe	19.27	−47.89	11.9	77.9	SL	10NE; 79
Xainza	0.78	−3.93	13.4	100.2	No	1SE; 379
Yuty	22.13	−34.05	10.4	49.3	DL	11NW; 233
	31.88	115.16	1.1	4.5	n/a	n/a
	32.58	113.97	1.3	7.5	n/a	n/a
	35.52	135.44	1.7	34.4	n/a	n/a
	−23.81	−110.33	2.2	7.6	No	17SE; 7
	26.41	−27.20	2.2	12.9	No	11NW; 92
	32.14	115.33	2.4	19.7	No	07SW; 3
	30.58	−47.45	2.4	16.4	No	04SW; 106
	33.14	112.92	2.7	18.5	No	07SW; 4
	31.14	117.52	2.8	23.3	No	07SW; 8
	33.54	111.93	2.8	11.3	No	06SE; 35
	−24.46	−111.68	2.9	12.8	No	17SE; 8
	36.88	124.33	3.2	20.3	DL	07SW; 94
	−34.05	134.56	3.2	40.0	No	29NW; 274
	56.97	−83.58	3.3	9.3	No	03NE; 36
	21.65	−29.22	3.3	20.7	No	11NW; 22
	35.46	−58.82	3.4	38.6	No	04SW; 66
	31.45	118.41	3.7	28.3	No	07SW; 9
	−45.57	−86.51	3.7	18.0	No	25NE; 166
	52.09	167.16	3.9	38.1	No	07NE; 13
	40.99	−61.36	4.0	24.2	No	04SW; 168
	−22.85	−112.48	4.2	36.3	No	17SE; 9
	−21.97	−75.83	4.3	25.6	SL	18SW; 74
	30.32	−46.64	4.3	29.0	No	04SW; 107
	31.80	114.37	4.5	35.8	No	07SW; 2
	25.78	−26.77	4.6	36.0	SL	11NW; 91
	32.39	111.32	4.8	29.1	No	06SE; 34
	16.84	156.37	5.1	29.0	SL	15NW; 37
	34.91	111.62	5.4	30.9	No	06SE; 70
	56.70	−84.79	5.7	27.8	DL	03NE; 35
	−21.03	−77.38	5.7	19.3	SL	18SW; 77
	31.49	116.30	5.9	35.9	DL	07SW; 7
	55.35	−106.44	6.0	113.3	DL	03NW; 108
	42.54	−51.08	6.0	41.9	No	04SW; 313
	34.20	109.64	6.1	38.9	No	06SE; 38
	−43.74	−87.20	6.1	20.3	No	25NE; 344
	−18.91	−76.29	6.2	26.1	SL	18SW; 128
	−42.45	101.16	6.4	64.0	Rd	28NE; 44
	42.11	−47.80	6.7	28.5	SL	04SW; 366
	−34.71	135.63	6.7	36.6	SL	29NC; 164
	44.05	−60.75	7.6	60.1	No	04SW; 290
	7.63	−5.19	7.7	29.7	No	1SE; 330
	−6.42	81.68	7.8	54.0	SL	21NE; 457
	−22.39	−172.70	8.0	33.6	SL	16SW; 417
	40.93	98.35	8.1	38.9	DL	06SE; 85
	22.57	−25.58	8.2	64.8	ML	11NW; 98
	−25.14	−136.61	8.6	45.4	SL	16SE; 433
	−42.23	−88.26	8.7	46.3	SL	25NE; 193
	16.22	155.14	8.8	51.1	ML	15NW; 36
	−38.01	16.49	8.8	55.8	DL	27NW; 191
	44.03	101.77	9.1	44.8	DL	06SE; 123
	40.23	−47.76	9.1	34.6	No	04SW; 117
	37.42	161.80	9.6	69.3	No	07SE; 77
	−23.25	7.28	10.3	44.1	No	20SW; 434
	38.52	99.25	10.6	70.6	DL	06SE; 83
	54.83	−93.40	10.7	53.3	DL	03NW; 63
	44.47	−156.91	10.8	53.9	DL	02SC;15
	−35.71	129.49	10.8	66.5	No	29SW; 540

Table 3 (*continued*)

Name	Latitude (°)	Longitude (°E)	Crater radius (km)	Dark halo radius (km)	Ejecta[a]	Barlow (2005) crater[a]
	27.97	−27.68	11.4	62.2	SL	11NW; 67
	41.55	166.77	12.0	136.3	ML	07SE; 51
	7.80	−0.37	12.2	76.1	ML	1SE; 318
	−31.41	−81.83	13.2	66.0	SL	25NE; 283
	36.55	−30.37	14.1	90.2	DL	04SC; 53
	−42.95	−86.60	15.9	34.5	No	25NE; 183
	40.81	−60.39	16.1	67.3	No	04SW; 167
	35.81	−40.75	18.5	110.6	DL	04SC; 43
	54.79	−75.27	19.8	153.1	No	03NE; 21
	19.23	169.91	21.1	113.2	No	15NE; 154
	12.86	99.63	22.8	63.8	ML	14SW; 319
	10.19	94.32	27.4	159.3	Di	14SW; 298
	12.14	105.14	30.5	141.0	ML	14SW; 262
	−32.03	140.79	32.2	168.5	Di	29NC; 195

[a] Barlow (2005).

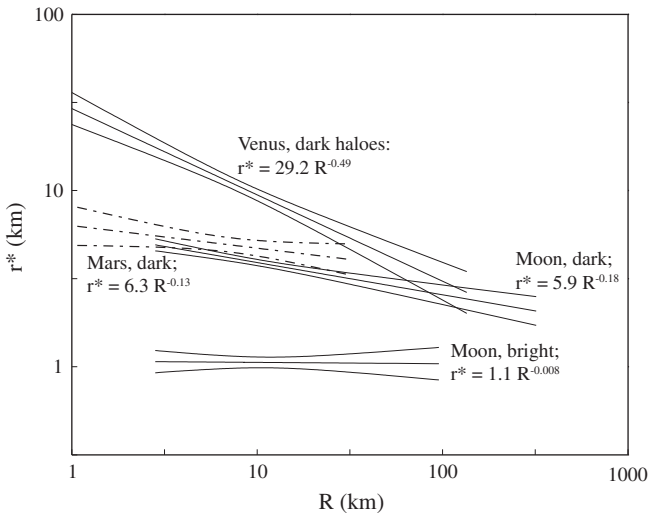

Fig. 6. Log–log regressions of fine ejecta run-out vs. crater radius for the Moon, Venus, and Mars. Run-out distance r^* is measured from crater rim and normalized by crater radius, R (see text). Regressions shown with 95% confidence intervals. Trends for all planets follow the form: $r^* = aR^b$. Lunar bright haloes: $N = 200$; lunar dark haloes: $N = 275$; martian dark haloes: $N = 88$; venusian dark haloes: $N = 196$.

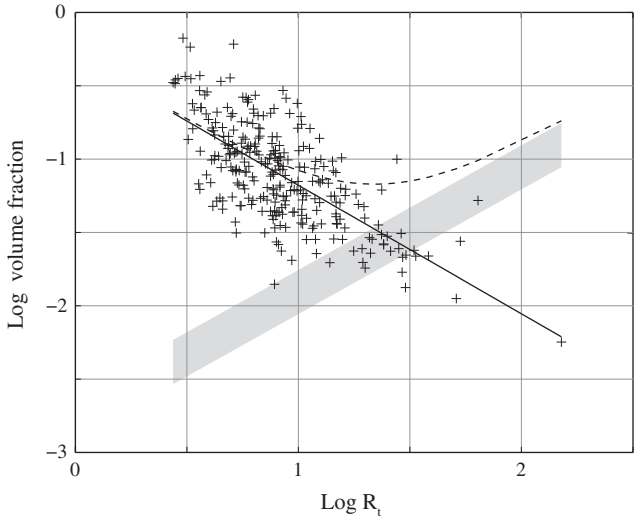

Fig. 7. Estimated lunar radar-dark halo volumes normalized to transient crater volumes (crosses; $V_H/V_t = 0.50\ r_c^{-0.88}$). Shaded region shows estimated bounds on impact melt volumes (Cintala and Grieve, 1998) $V_m/V_t = (1-2) \times 10^{-4}\ r_c^{0.85}$. Dashed curve is the sum of fine ejecta and melt volumes calculated according to these two power laws.

Again, additional work is required to determine whether vapor plume-deposited haloes would scale with crater size according the observed relationship.

4. Discussion

Our results show that lunar radar-bright haloes scale with crater size according to a ballistic emplacement relationship, and venusian radar-dark halo scaling is consistent with atmospheric entrainment; both mechanisms apply to late-time deposition of material originating within the crater cavity. We conclude that the haloes on both planets are intrinsic impact features, and are not simply the result of modification of pre-existing regolith. For the lunar case, we cannot determine from current observations whether the radar-dark halo material consists of bedrock comminuted during impact, or of fine regolith materials that have been sorted and redistributed. In either case, the observation that the radar-dark haloes have precipitous boundaries and minimum thicknesses on the order of 7 m indicates that ejecta leaving the crater cavity reach a particular maximum crater-scaled range, and accumulate there, rather than continuing to thin with distance from the crater rim. This constrains the range of ejection velocities, and thus, the particles' ejection positions within the excavation cavity. We also cannot currently determine the dark haloes' particle sizes beyond the upper bound ($d \leqslant 1$ cm) placed by the haloes' low radar returns at 12.6-cm wavelength. However, a quantitative estimate may be possible using new thermal IR data from the Diviner lunar radiometer aboard the Lunar Reconnaissance Orbiter (Paige et al., 2009); this will help to determine the origin of the dark halo particles and constrain the processes that govern their emplacement.

For Mars, the discrepancy between our observed halo scaling and that predicted for partial entrainment in curtain-generated vortices suggest that the low-T halo material was not emplaced by that mechanism. Those predictions seem to work well for martian ramparts, whose sizes scale as $R^{1/2}$ (Schultz, 1992a). The particles that form the low nighttime temperature haloes discussed here, however, are smaller than those that comprise the ramparts. It is not surprising that smaller particles travel farther than larger ones, and therefore, are emplaced beyond the ramparts; but it is surprising that the crater-scaled halo sizes decrease with increasing crater size similarly to the ballistic lunar case. It seems clear from these observations that low-temperature halo-forming ejecta are emplaced by a different mechanism from those that form ramparts. Key observations are that the low-temperature haloes are

larger than other types of ejecta deposits, and commonly extend past the ends of ejecta lobes; they are characterized by distinct radial texture, with some showing wispy or digitate margins, or streamers that continue out to large distances; they scale with crater size in a similar fashion to the ballistically emplaced lunar haloes; and that they have persisted for geologically significant lengths of time without being erased by post-impact processes such as aeolian erosion. Clearly, it is probable that some of the fine material comprising the haloes has been removed, so that we cannot now measure their original extent. However, there is no reason to expect that removal of halo material would occur in such a way as to drastically change the slope of the scaling relationship.

It may be that the fine halo-forming ejecta are emplaced by a base surge mechanism prior to arrival of curtain-generated vortices, as suggested for outer ejecta layers for DLE craters by Boyce and Mouginis-Mark (2006). However, the haloes' strong radial fabric and the delicate, wispy morphology of distal halo margins suggest a wind-driven mechanism. Rather than invoking a "late-time" mechanism for their emplacement (such as curtain-driven vortices or base surge), we favor the "early-time" mechanism whereby expansion of the impact-generated vapor plume gives rise to the necessary high-speed winds. The results of Wrobel et al. (2006), which assumed relatively conservative values for the degree of energy partitioning into the atmosphere, showed that such a process can easily produce winds of sufficient velocity and over a sufficient distance from the point of impact to distribute fine ejecta as observed. Furthermore, their modeling predicted that dissipation of some of the impact energy as heat would result in temperatures well above the melting point of subsurface volatiles such as water ice; this would provide additional vapor and increase the strength of the dispersive effect of the expanding plume. It should be noted that the morphology of the low-temperature haloes does not, we feel, require suspension and transportation of ejecta by water or ice as has been invoked for formation of layered ejecta lobes (e.g., Komatsu et al., 2007; Senft and Stewart, 2008). However, the presence of water in the vapor plume could, as suggested by Wrobel et al. (2006), result in an erosion-resistant armor that might account for the persistence of low-temperature haloes for long periods of time. Such deposits might even survive burial and exhumation. If so, their spatial distribution might offer important insight into the conditions under which they formed.

In conclusion, our results provide new information about the production and emplacement of highly comminuted fragmental debris in planetary impacts. For the Moon, the use of large sample sizes for scaling observations confirms earlier estimates for continuous ejecta scaling based on empirical studies that combined small-scale experiments, terrestrial explosion craters, and a small number of lunar craters (e.g., Short and Forman, 1972; McGetchin et al., 1973). The venusian results provide robust observational evidence for atmospheric ejecta entrainment, and constrain the ejecta cloud density. Finally, the results for Mars are relevant to our understanding of the interaction between the martian atmosphere and fine sediment, which is important for studies of aeolian processes.

Acknowledgments

We thank Nadine Barlow and Goro Komatsu for constructive reviews, which greatly improved the quality of this paper. Taronish Pithawala and John Koziar assisted with halo identification. This work was supported by a grant from the Natural Sciences and Engineering Research Council of Canada to R.R.G., and by the NASA Planetary Astronomy and PGG Programs. Arecibo Observatory is part of the National Astronomy and Ionosphere Center, operated by Cornell University under a cooperative agreement with the NSF. The Green Bank Telescope is part of the National Radio Astronomy Observatory, an NSF facility operated under cooperative agreement by Associated Universities, Inc.

References

Baratoux, D., Mangold, N., Pinet, P., 2005. Thermal properties of lobate ejecta in Syrtis Major, Mars: Implications for the mechanisms of formations. J. Geophys. Res. 110, E04011. doi:10.1029/2004JE002314.

Barlow, N.G., Boyce, J.M., Costard, F.M., Craddock, R.A., Garvin, J.B., Sakimoto, S.E.H., Kuzmin, R.O., Roddy, D.J., Soderblom, L.A., 2000. Standardizing the nomenclature of martian impact crater ejecta morphologies. J. Geophys. Res. 105, 26733–26738.

Barlow, N.G., 2005. A review of martian impact crater ejecta structures and their implications for target properties. Geol. Soc. Am. Spec. Papers 384, 433–442. doi:10.1130/0-8137-2384-1.433.

Barnouin-Jha, O.S., 1998. Modeling Atmospheric Entrainment and Transport of Impact Ejecta. PhD thesis, Providence, Brown University.

Barnouin-Jha, O.S., Schultz, P.H., 1996. Ejecta entrainment by impact-generated ring vortices: Theory and experiments. J. Geophys. Res. 101, 21099–21115.

Barnouin-Jha, O.S., Schultz, P.H., Lever, J.H., 1999. Investigating the interactions between an atmosphere and an ejecta curtain. 2. Numerical experiments. J. Geophys. Res. 104, 27117–27131.

Boyce, J.M., Mouginis-Mark, P.J., 2006. Martian craters viewed by the Thermal Emission Imaging System instrument: Double-layered ejecta craters. J. Geophys. Res. 111, E10005. doi:10.1029/2005JE002638.

Campbell, D.B., Stacy, N.J.S., Newman, W.I., Arvidson, R.E., Jones, E.M., Musser, G.S., Roper, A.Y., Schaller, C., 1992. Magellan observations of extended impact crater related features on the surface of Venus. J. Geophys. Res. 97, 16249–16277.

Campbell, B.A., Campbell, D.B., Margot, J.L., Ghent, R.R., Nolan, M., Chandler, J., Carter, L.M., Stacy, N.J.S., 2007. Focused 70-cm wavelength radar mapping of the Moon. IEEE Trans. Geosci. Rem. Sens. 45, 4032–4042.

Christensen, P., Gorelick, N., Anwar, S., Dickenshied, S., Edwards, C., Engle, E., 2007. New insights about Mars from the creation and analysis of Mars global datasets. In: Am. Geophys. Union Fall Meeting 2007. Abstract #P11E-01.

Cintala, M.J., Grieve, R.A.F., 1998. Scaling impact-melt and crater dimensions: Implications for the lunar cratering record. Meteor. Planet. Sci. 33 (4), 889–912.

Fergason, R.L., Christensen, P.R., Kieffer, H.H., 2006. High-resolution thermal inertia derived from the Thermal Emission Imaging System (THEMIS): Thermal model and applications. J. Geophys. Res. 111. doi:10.1029/2006JE002735.

Gault, D.E., Hoerz, F., Brownlee, D.E., Hartung, J.B., 1974. Mixing of the lunar regolith. Proc. Lunar Sci. Conf. 5, 3, 2365–2386. Pergamon Press, New York.

Gault, D.E., Guest, J.E., Murray, J.B., Dzurisin, D., Malin, M.C., 1975. Some comparisons of impact craters on Mercury and the Moon. J. Geophys. Res. 80, 2444–2460.

Ghent, R.R., Leverington, D.W., Campbell, B.A., Hawke, B.R., Campbell, D.B., 2005. Earth-based observations of radar-dark crater haloes on the Moon: Implications for regolith properties. J. Geophys. Res. 110. doi:10.1029/2004JE002366.

Ghent, R.R., Campbell, B.A., Hawke, B.R., Campbell, D.B., 2008. Earth-based radar data reveal extended deposits of the Moon's Orientale basin. Geology 36, 343–346.

Guest, J.E., Spudis, P.D., 1985. The Aristarchus impact event and the effects of target material. Geol. Mag. 122, 317–327.

Herrick, R.R., Sharpton, V.L., Malin, M.C., Lyons, S.N., Feely, K., 1997. Morphology and morphometry of impact craters. In: Bougher, W., Hunten, D.M., Phillips, R.J. (Eds.), Venus II. Univ. of Arizona Press, Tucson, pp. 1015–1046.

Komatsu, G., Ori, G.G., Rossi, A.P., Di Lorenzo, S., Neukum, G., 2007. Combinations of processes responsible for martian impact crater "layered ejecta structures" emplacement. J. Geophys. Res. 112 (E6). doi:10.1029/2006JE002787 (Barlow, 2005).

Lucey, P.G., Hawke, B.R., Pieters, C.M., Head, J.W., McCord, T.B., 1986. A compositional study of the Aristarchus region of the Moon using near-infrared reflectance spectroscopy. J. Geophys. Res. 91, D344–D354.

Melosh, H.J., 1989. Impact Cratering: A Geologic Process. Oxford Monographs on Geology and Geophysics, vol. 11. Oxford University Press, New York.

McGetchin, T.R., Settle, M., Head, J.W., 1973. Radial thickness variation in impact crater ejecta: Implications for lunar basin deposits. Earth Planet. Sci. Lett. 20, 226–236.

Moore, H.J., Hodges, C.A., Scott, D.H., 1974. Multiringed basins – Illustrated by Orientale and associated features. Proc. Lunar Sci. Conf. 5, 1, 71–100. Pergamon Press, Inc., New York.

Oberbeck, V.R., 1975. The role of ballistic erosion and sedimentation in lunar stratigraphy. Rev. Geophys. Space Phys. 13 (2), 337–362.

Paige, D.A., and 22 colleagues, 2009. The Lunar Reconnaissance Orbiter diviner lunar radiometer experiment. Space Sci. Rev. doi:10.1007/s11214-009-9529-2.

Pike, R.J., 1977, Size-dependence in the shape of fresh impact craters on the Moon. In: Impact and Explosion Cratering. Planetary and Terrestrial Implications: Proceedings of the Symposium on Planetary Cratering Mechanics. Pergamon Press, Inc., New York, pp. 489–509.

Presley, M.A., Christensen, P.R., 1997. Thermal conductivity measurements of particulate materials. 2. Results. J. Geophys. Res. 102, 6551–6566.

Presley, M.A., Craddock, R.A., 2006. Thermal conductivity measurements of particulate materials: 3. Natural samples and mixtures of particle sizes. J. Geophys. Res. 111. doi:10.1029/2006JE002706.

Schaber, G.G., Strom, R.G., Moore, H.J., Soderblom, L.A., Kirk, R.L., Chadwick, D.J., Dawson, D.D., Gaddis, L.R., Boyce, J.M., Russell, J., 1992. Geology and distribution

of impact craters on Venus: What are they telling us? J. Geophys. Res. 97, 13257–13301.
Schultz, P.H., Gault, D.E., 1985. Impact-induced vaporization: Effect of impact angle and atmospheric pressure. Lunar Planet. Sci. XVI, 740–741.
Schultz, P.H., 1988. Impact vaporization of volatile-rich targets: Experimental results and implications. Lunar Planet. Sci. 19, 1039–1040 (abstracts).
Schultz, P.H., 1992a. Atmospheric effects on ejecta emplacement. J. Geophys. Res. 97, 11623–11662.
Schultz, P.H., 1992b. Atmospheric effects on ejecta emplacement and crater formation on Venus from Magellan. J. Geophys. Res. 97, 16183–16248.
Senft, L.E., Stewart, S.T., 2008. Impact crater formation in icy layered terrains on Mars. Meteor. Planet. Sci. 43 (12), 1993–2013. doi:10.1111/j.1945-5100.2008.tb00657.x.
Short, N.M., Forman, M.L., 1972. Thickness of impact crater ejecta on the lunar surface. Modern Geol. 3, 69–91.
Thompson, T.W., Campbell, B.A., Ghent, R.R., Hawke, B.R., Leverington, D.W., 2006. Radar probing of planetary regoliths: An example from the northern rim of Imbrium basin. J. Geophys. Res. 111. doi:10.1029/2005JE002566.
Wrobel, K., Schultz, P.H., Crawford, D., 2006. An atmospheric blast/thermal model for the formation of high-latitude pedestal craters. Meteor. Planet. Sci. 41 (10), 1539–1550.